Moveout analysis of wave-equation extended images

Tongning Yang and Paul Sava
Center for Wave Phenomena, Colorado School of Mines

ABSTRACT
Conventional velocity analysis applied to images produced by wave-equation migration with a cross-correlation imaging condition makes use either of moveout information from space-lags or of focusing information from time-lags. However, more robust velocity estimation methods can be designed to take advantage simultaneously of the moveout and focusing information provided by the migrated images. Such joint velocity estimation requires characterization of the moveout surfaces defined jointly for space- and time-lag common-image gathers. Such surfaces estimated for single events (shots) are non-planar but they reduce naturally to the conventional space-lag and time-lag moveout functions. The superposition of those surfaces for many experiments (shots) in a common-image gather forms a shape which can be characterized as a "light-cone" in the lag space. When imaged with correct velocity, the focus of the light cone is located at the correct image depth and at zero space- and time-lags. When imaged with incorrect velocity, the focus of the light cone shifts both in depth and along the time-lag axis. The characteristics of the light cones are directly related to the quality of the velocity model, thus their analysis provides a rich source of information for velocity model building. Joint migration velocity analysis technique exploiting the entire information provided by the extended imaging condition has the potential to benefit from the combination of the robustness of depth focusing analysis and of the high resolution of conventional semblance analysis.

Key words: wave-equation, extended imaging, focusing, semblance

1 INTRODUCTION

A key challenge for imaging in complex geology is an accurate determination of the velocity model in the area under investigation. Migration velocity analysis is based on the principle that image accuracy indicators are optimized when data are correctly imaged. A common procedure for migration velocity analysis is to examine the alignment of images created with data from many complementary experiments. An optimal choice for image analysis in complex areas is the angle domain which is free of complicated artifacts present in surface offset gathers (Stolk & Symes, 2004). If images constructed by illuminating a point from various directions are aligned, then the velocity model used for imaging is said to be accurate. This idea is usually referred to as the *semblance principle* (Yilmaz, 2001) and it represents the foundation of most velocity analysis methods in use today.

Often, semblance analysis is performed in the angle domain. Several methods have been proposed for angle decomposition (Sava & Fomel, 2003b,a; Fomel, 2004; Biondi & Symes, 2004). All these procedures require decomposition of extrapolated wavefields or of migrated images in components that are related to the reflection angles. This imaging procedure requires the application of an *extended imaging condition* (Sava & Fomel, 2006) which implements a point-by-point comparison of the source and receiver wavefields extrapolated from the surface. In general, the comparison is done using simple image processing procedures applied at every location in the subsurface. If the source and receiver wavefields match each-other, then their cross-correlation maximizes at zero lag in space and time; otherwise, their cross-correlation does not maximize at zero lag indicating wavefield reconstruction error which may have different causes, e.g., velocity inaccuracy.

The source and receiver wavefields used for imaging are 4D objects, function of space coordinates and time (or frequency). For simplicity, we discuss in this paper only time-domain imaging, although our analysis applies equally well to frequency domain imaging. For such 4D objects, the images obtained by extended imaging conditions are characterized in general by a 3D space-lag vector and a 1D time-lag. The

images constructed with space- and time-lags can be decomposed function of reflection angles using geometric relations between incident and reflected rays (Sava & Fomel, 2006).

Conventional migration velocity analysis exploits separately either space-lag information, by *semblance analysis* (Sava & Biondi, 2004a,b; Shen et al., 2005), or the time-lag information, by *depth focusing analysis* (Faye & Jeannot, 1986; MacKay & Abma, 1992, 1993; Nemeth, 1995, 1996; Sava & Fomel, 2006). However, we suggest here that a more robust velocity analysis approach combines the information provided by the space and time-lags and optimize migrated images using all available information. This way, we can leverage at the same time the robustness of depth focusing analysis and the high resolution of semblance analysis.

In this paper, we analyze the moveout function for common-image gathers constructed by extended imaging conditions applied after conventional wavefield extrapolation. We first derive the analytic expression of the moveout function for space- and time-lag extended imaging conditions. Next, we focus on the common-image gathers in multi-shot experiments and quantitatively analyze their characteristics, especially the features related to velocity error. Finally, simple and complex synthetic examples are presented to verify the derived analytic moveout functions and to illustrate the application of this technique in complex geologic models.

2 WAVE-EQUATION IMAGING CONDITIONS

Under the single scattering assumption, the seismic migration procedure consists of two main steps: wavefield reconstruction and imaging condition. Wavefield reconstruction involves constructing solutions to a wave-equation with recorded data as initial and boundary condition. Various numeric solutions for the acoustic wave-equation can be chosen depending on the specific requirements of cost and accuracy. However, regardless of the specific implementation, the reconstruction of both source and receiver wavefields is similar. In a known background velocity model, we forward propagate from the source location to obtain the source wavefield, and backward propagate the recorded seismic data to obtain the receiver wavefield. The reconstructed source and receiver wavefields can be defined as four-dimensional objects function of spatial location $\mathbf{x} = (x, y, z)$ and time t,

$$u_s = u_s(\mathbf{x}, t) , \quad (1)$$

$$u_r = u_r(\mathbf{x}, t) , \quad (2)$$

where u_s and u_r stand for the source and receiver acoustic wavefields, respectively.

An imaging condition is designed to extract from these reconstructed wavefields the locations where reflectors occur in the subsurface. The image $r(\mathbf{x})$ is obtained by evaluating the match between the reconstructed source and receiver wavefields at every location in the subsurface. A conventional imaging condition (Claerbout, 1985) forms an image as the zero cross-correlation lag between the source and receiver wavefields:

$$r(\mathbf{x}) = \sum_t u_r(\mathbf{x}, t)\, u_s(\mathbf{x}, t) \quad (3)$$

An alternative extended imaging condition (Rickett & Sava, 2002; Sava & Fomel, 2006) generalizes the conventional imaging condition by preserving into the output image the information from non-zero cross-correlation lags:

$$r(\mathbf{x}, \boldsymbol{\lambda}, \tau) = \sum_t u_s(\mathbf{x} - \boldsymbol{\lambda}, t - \tau)\, u_r(\mathbf{x} + \boldsymbol{\lambda}, t + \tau) . \quad (4)$$

The quantities $\boldsymbol{\lambda}$ and τ represent the spatial and temporal cross-correlation lags between the source and receiver wavefields. Like the conventional imaging condition, the extended imaging condition also evaluates the match between the wavefields by their cross-correlation, but it preserves in the output the information corresponding to non-zero cross-correlation space- and time-lags. Due to the existence of the lags, the resulting images are in fact series of images obtained with different extension at each subsurface location $\mathbf{x}$. We refer to those image series as wave-equation extended images. Such image hypercubes can help us analyze the accuracy of the reconstructed wavefields. If the local cross-correlation between the source and receiver wavefields maximizes at zero lag on all four dimensions, then those wavefields are extrapolated correctly. If this is not true, then we may conclude that the wavefield reconstruction is incorrect, indicating incorrect velocity or incorrect wavefield extrapolation or irregular illumination, or the failure of the single scattering assumption, e.g., due to the presence of multiples. In this research, we consider that the errors in wavefield reconstruction are caused by incorrect velocity only.

3 MOVEOUT ANALYSIS FOR EXTENDED IMAGES – POINT SOURCE

The shape of the extended images can be studied by analyzing common-image gathers (CIG). A reflection event analyzed in a CIG is represented by a multi-variable function $z = z(\boldsymbol{\lambda}, \tau)$. For the purpose of migration velocity analysis, it is necessary to understand the correct shape of this function, often referred to as "moveout" by analogy with surface seismic data. Characterizing the moveout of the events present in extended CIGs for the cases of correct and incorrect velocity is essential for the understanding of their use in a subsequent tomographic procedure.

Consider the reflection geometry depicted in Figure 1: the unit vector $\mathbf{n} = \{n_x, n_y, n_z\}$ and the distance d identify the position of a reflection plane relative to the seismic source **S**; the vector $\mathbf{c} = \{c_x, c_y, 0\}$ identifies the fixed horizontal position of a CIG relative to the source position, the vector $\mathbf{z} = \{0, 0, z\}$ represents the depth of the image constructed by the imaging condition. We consider here the case when extended imaging condition are computed function of horizontal space-lag $\boldsymbol{\lambda} = \{\lambda_x, \lambda_y, 0\}$ and time-lag τ, but the same logic applies to the more general case when the space-lag $\boldsymbol{\lambda}$ is three-dimensional.

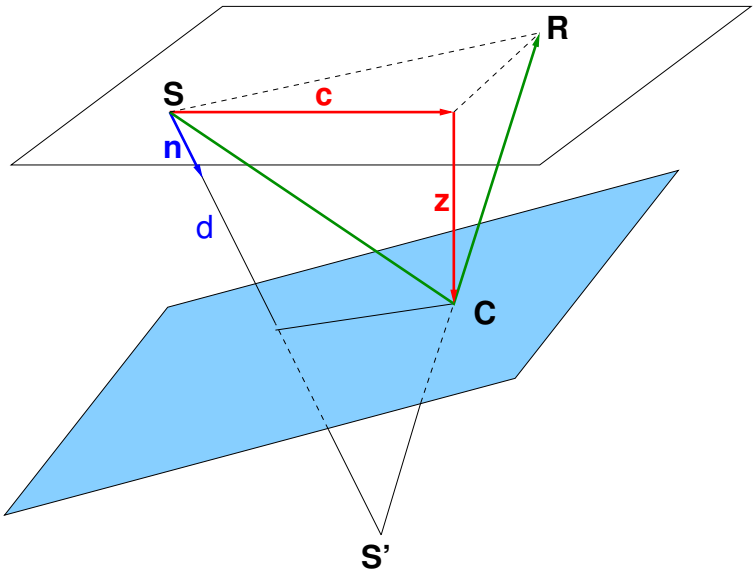


Figure 1. Geometry of a reflection experiment. **S**, **R** and **C** identify the positions of the source, receiver and image, respectively. The reflector is located at distance d from the source position in the direction of the vector **n**. The position of the CIG relative to the source is indicated by the vectors **c** and **z**.

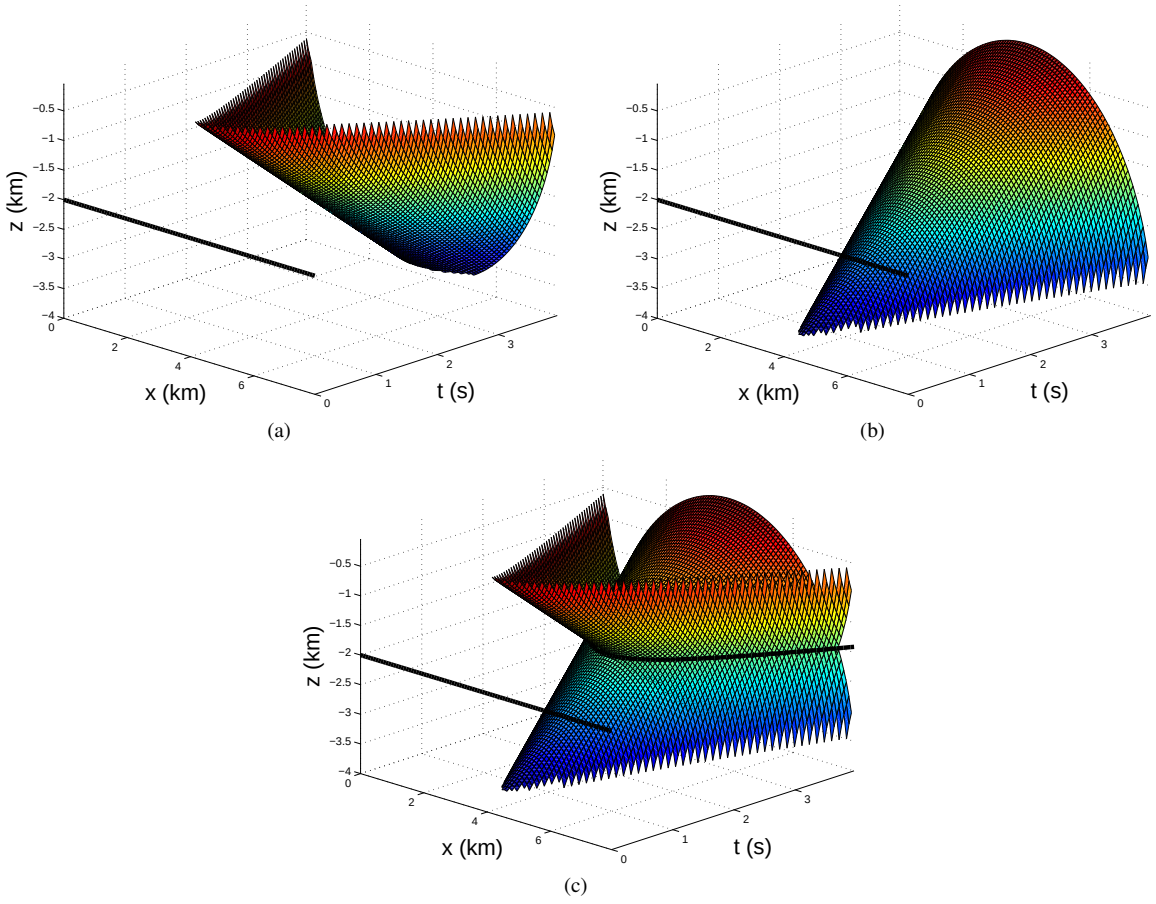


Figure 2. (a) Source wavefield in a homogeneous medium represented by a cone in space-time. (b) Receiver wavefield in a homogeneous medium represented by the mirror image of the source wavefield relative to the reflector. (c) Intersections of the source and receiver wavefields reconstructed with correct velocity. The projection of the intersection onto Cartesian spatial coordinates indicates the position of the reflector.

Under the assumption of homogeneous media, a wavefield characterizing wave propagation from a point can be represented by a cone in space-time. The source wavefield is represented by a cone with the origin at zero time and at the source location on the surface, as shown in Figure 2(a). Likewise, we construct the receiver wavefield as the mirror image of the source wavefield relative to the reflector present in the image, as shown in Figure 2(b). Using this description of the seismic wavefields, we can represent the source and receiver wavefields in space-time by the analytic expressions:

$$\|\mathbf{c}+\mathbf{z}\| = vt\ , \tag{5}$$

$$\|\mathbf{c}+\mathbf{z}-2d\mathbf{n}\| = vt\ , \tag{6}$$

where v is the velocity of the medium, t is the propagation time of the wavefield, $\mathbf{z}=\{0,0,z\}$ with z representing the depth of the image. As discussed before, the imaging conditions identify the position of the reflector by evaluating the match between source and receiver wavefields. In other words, an image forms at the space positions where the source and receiver wavefields intersect. Mathematically, this condition is equivalent to identifying the positions which are a solution to the system given by equations 5-6, i.e. by solving the system for the reflection depth z at coordinates $\{c_x,c_y\}$. Figures 2(a)-2(c) illustrate this procedure. Figure 2(a) represents the source wavefield, Figure 2(b) represents the receiver wavefield. The cones are symmetric relative to the reflector which is indicated by the thick line in the $x-z$ plane. The intersection of the cones occurs at different times. However, the locations of the intersections are consistent with the position of the reflector since their projection on the $x-z$ plane matches the reflector perfectly.

Likewise, the extended imaging condition seeks to find the intersections between the source and receiver wavefields. However, this procedure is different because both wavefields are shifted by quantities corresponding to the space- and time-lags of the cross-correlation. Since we construct the extended images for the same subsurface location, we keep the CIG coordinate $\mathbf{c}$ fixed. The shifted wavefields are function of the space quantity $\boldsymbol{\lambda}=\{\lambda_x,\lambda_y,0\}$ and time quantity τ. Thus, the extended imaging condition is represented by the system

$$\|\mathbf{c}+\mathbf{z}+\boldsymbol{\lambda}\| = v\left(t+\tau\right)\ , \tag{7}$$

$$\|\mathbf{c}+\mathbf{z}-2d\mathbf{n}-\boldsymbol{\lambda}\| = v\left(t-\tau\right)\ . \tag{8}$$

The application of the extended imaging condition in equation 4 is equivalent to solving equations 7-8. The solution represents the moveout function $z=z\left(\boldsymbol{\lambda},\tau\right)$ at fixed CIG coordinates $\mathbf{c}=\{c_x,c_y,0\}$. This moveout function describes how the depth z of the image changes with the variation of the space- and time-lags.

A formal solution to the system of equations 7-8 leads to the following expression of the depth z at the CIG coordinates $\{c_x,c_y\}$ function of space- and time-lags:

$$z\left(\boldsymbol{\lambda},\tau\right)=\left(dn_z\right)K+v\tau\sqrt{K^2+\frac{\|\mathbf{c}+\boldsymbol{\lambda}\|^2}{\left(dn_z\right)^2-\left(v\tau\right)^2}}\ , \tag{9}$$

where

$$K=1-\frac{\left(\mathbf{c}\cdot\mathbf{n}\right)d-\left(n_x^2+n_y^2\right)d^2+\left(\mathbf{c}-d\mathbf{n}\right)\cdot\boldsymbol{\lambda}}{\left(dn_z\right)^2-\left(v\tau\right)^2}\ . \tag{10}$$

Equation 9 represents the moveout function characterizing the shape of the extended images.

To better understand the characteristics of the moveout function, we analyze two special cases of the extended images. First case corresponds to imaging with space-lags only, e.g. $\tau=0$, which is the slice of the surface at zero time-lag. Since the square-root term vanishes owing to the zero time-lag, we obtain a linear moveout function relative to space-lag parameters. The coefficient depends on the reflection angles on the reflector, which justifies the angle decomposition methods based on the slant-stacks applied to space-lag CIGs (Sava & Fomel, 2003b; Biondi & Symes, 2004; Fomel, 2004). The second case corresponds to imaging with time-lag only, e.g. $\boldsymbol{\lambda}=0$, which is the slice of the surface at zero space-lags. For this special case, the moveout function is still nonlinear.

As discussed before, the goal of our research is to understand the relationship between features of extended images and velocity error. A quantitative analysis of the influence of the velocity error on the extended images is required to achieve this goal. When incorrect velocity is used for wavefield reconstruction, the wavefields are incorrectly extrapolated. Consequently, applying the imaging condition produces distorted images which deviate from correct spatial locations. As a result, we first have to understand the influence of the incorrect velocity model on the reconstructed wavefields because the analytic descriptions of the source and receiver wavefields are the key step for deriving the moveout function. To simplify the problem, we denote the migration velocity $v_m=\rho_v v$, where ρ_v is a constant indicating the degree by which the migration velocity is different from the correct velocity.

The source wavefield is reconstructed as in the preceding situation, except that we use the migration velocity instead of the correct one. The wavefields are represented by cones with different radii compared to the ones used for the case of correct velocity. Figure 3(a) shows the source wavefield reconstructed with incorrect velocity. The wavefield is described by the equation

$$\|\mathbf{c}+\mathbf{z}\| = v_m t\ . \tag{11}$$

For the receiver wavefield, the situation is more complicated. Unlike the source wavefield, the receiver wavefield is reconstructed by backward propagation of the recorded data. In other words, we reconstruct the cone representing the source wavefield from its origin while we reconstruct the cone representing the receiver wavefield from its depth slice recorded on the surface. If correct velocity is used, the cone for the receiver wavefield obtained is exactly the image of the cone for source wavefield, which means both cones are symmetric in space and have the same trigger time. In contrast, if incorrect velocity is used, the cone representing the receiver wavefield changes its radius just as was the case for the source wavefield. Furthermore, the origin of the cone departs from its true position in space and time, and the symmetry axis between the

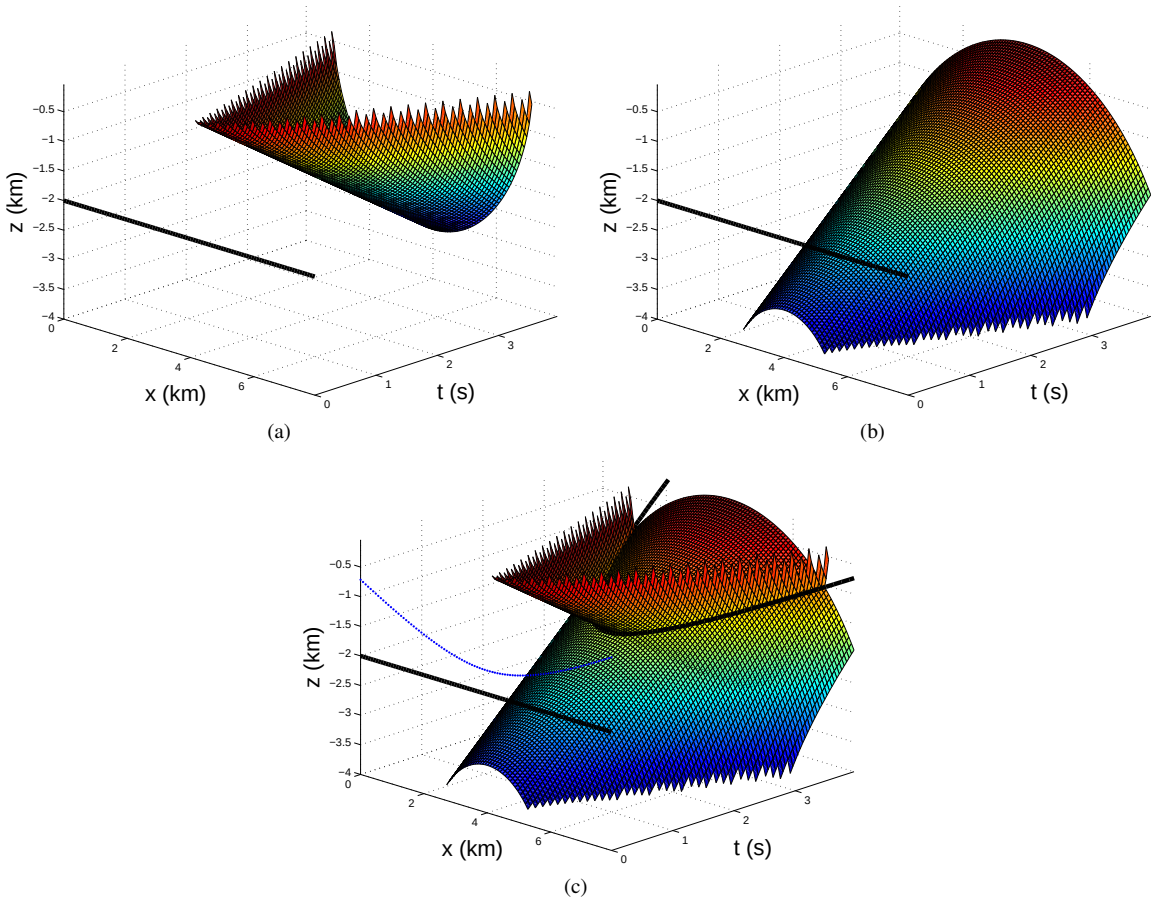


Figure 3. (a) Source wavefield in a homogeneous medium constructed using an incorrect velocity. The wavefield forms a cone in space-time and has a different shape compared with the wavefield constructed with the correct velocity model. (b) Receiver wavefield in a homogeneous medium constructed using an incorrect velocity. The wavefield forms a cone in space-time and has a different shape relative to the wavefield constructed in the correct velocity, and is also shifted along the time axis. (c) Intersections of the source and receiver wavefields reconstructed with incorrect velocity. The curved dash line, which is the projection of the intersection onto Cartesian spatial coordinates, indicates the position of the reflector. The image is distorted compared to the case when the correct velocity model is used.

two cones deviate from their true spatial location. In summary, the receiver wavefield reconstructed using incorrect velocity is represented by a cone with a different radius, origin and symmetry axis.

As the receiver wavefield shifts in time, the reconstructed source and receiver wavefields are not generated at the same time. It is necessary to introduce a new variable to describe such a deviation. Using the concepts of focusing depth d_f and migration depth d_m (MacKay & Abma, 1992), we have $d_f = d/\rho_v$, $d_m = d\rho_v$, where ρ_v is the constant velocity scaling factor. We thus define the deviation as focusing delay t_d, which is quantified by the following formula:

$$t_d = \frac{d_f - d_m}{v_m} = \frac{d(1-\rho_v^2)}{v\rho_v^2} \ . \tag{12}$$

If the velocity is correct, the focusing depth and migration depth are identical and equal to the true depth of the reflection, thus the focusing delay vanishes.

As the receiver wavefield also shifts in space, the symmetry between both wavefields is maintained but the symmetry plane changes. The plane defined by $d\mathbf{n}$ in the case of correct velocity now becomes $d_f\mathbf{n}_m$, where d_f is the focusing depth of the reflection point, and $\mathbf{n}_m$ is a new normal vector which is a function of source-receiver location, correct normal $\mathbf{n}$ and the migrated velocity v_m. With this notation, the receiver wavefield is given by

$$\|\mathbf{c} + \mathbf{z} - 2d_f\mathbf{n}_m\| = v_m\,(t + 2t_d) \ . \tag{13}$$

Figure 3(b) shows the receiver wavefield in the case of horizontal reflector when v_m is smaller than v.

Solving the system of equations 11-13, we obtain the coordinates of the image when the incorrect velocity is used for imaging, as shown in 3(c). This solution is equivalent to applying the conventional imaging condition and finding the intersections between the incorrectly reconstructed source and receiver wavefields:

$$z\,(\mathbf{c}) = (d_f n_{mz})\,K - v_m t_d \sqrt{K^2 + \frac{\|\mathbf{c}\|^2}{(d_f n_{mz})^2 - (v_m t_d)^2}} \ , \tag{14}$$

where quantity K is defined by

$$K = 1 - \frac{(\mathbf{c}\cdot\mathbf{n}_m)\,d_f - \left(n_{mx}^2 + n_{my}^2\right) d_f^2}{(d_f n_{mz})^2 - (v_m t_d)^2} \ . \tag{15}$$

Depending on the ratio between the migrated velocity and true velocity, the term t_d can be positive or negative value.

Likewise, we may introduce the space and time-lags and obtain the expression for the shifted source and receiver wavefields for the case of imaging with incorrect velocity:

$$\|\mathbf{c} + \mathbf{z} + \boldsymbol{\lambda}\| = v_m\,(t + \tau) \ , \tag{16}$$

$$\|\mathbf{c} + \mathbf{z} - 2d_f\mathbf{n}_m - \boldsymbol{\lambda}\| = v_m\,(t + 2t_d - \tau) \ . \tag{17}$$

Solving this system gives the expression for the moveout surface function of space-lag $\boldsymbol{\lambda}$ and time-lag τ for incorrect velocity

$$z\,(\boldsymbol{\lambda},\tau) = (d_f n_{mz})\,K + v_m\,(\tau - t_d)\sqrt{K^2 + \frac{\|\mathbf{c}+\boldsymbol{\lambda}\|^2}{(d_f n_{mz})^2 - v_m^2\,(\tau - t_d)^2}} \ , \tag{18}$$

where quantity K is defined by

$$K = 1 - \frac{(\mathbf{c}\cdot\mathbf{n}_m)\,d_f - \left(n_{mx}^2 + n_{my}^2\right) d_f^2 + (\mathbf{c} - d_f\mathbf{n}_m)\cdot\boldsymbol{\lambda}}{(d_f n_{mz})^2 - v_m^2\,(\tau - t_d)^2} \ . \tag{19}$$

Comparing the moveout function in equation 18 to the moveout function in equation 9, we notice that the equations share a similar form, although the formula corresponding to the incorrect velocity model is more complicated. The complexity arises from the additional term t_d, as well as from the fact that d, v and $\mathbf{n}$ are replaced by d_f, v_m and $\mathbf{n}_m$. Owing to the existence of t_d, the square-root term is preserved when $\tau = 0$ thus the space-lag moveout function now has a nonlinear dependence on the variables. This characteristic may provide information about the accuracy of the velocity model.

4 MOVEOUT ANALYSIS FOR EXTENDED IMAGES – PLANE-WAVES

The analytic results discussed in the preceding sections have complicated forms, which prevents the formulas from being useful in practice. On the other hand, the moveout functions are derived based on the assumption of homogeneous media. Therefore, we must reduce the complexity of moveout functions and generalize the analysis to inhomogeneous media.

Figure 4 illustrates a seismic reflection occurring in an inhomogeneous medium, as indicated by the curved wave paths. The wavefield in such a medium can have arbitrary geometric shape rather than a simple cone, thus we cannot describe the wavefields using analytic formulas and derive analytic moveout functions. However, if we restrict the observation to the immediate vicinity of the reflection point, we can approximate the irregular wavefront by a plane. In other words, for inhomogeneous media, although the shapes of wavefronts are arbitrary, they can be approximated as plane-waves in the vicinity of the reflection point. Using the same geometry shown in Figure 1, the plane-wave wavefields are described as:

$$\mathbf{p}_s\cdot\mathbf{x} = vt \ , \tag{20}$$

$$\mathbf{p}_r\cdot(\mathbf{x} - 2d\mathbf{n}) = vt \ , \tag{21}$$

where $\mathbf{p}_s$ and $\mathbf{p}_r$ are the unit direction vectors of the source and receiver plane-waves respectively, $\mathbf{x}$ is the vector sum of $\mathbf{c}$ and $\mathbf{z}$. We can also obtain the shifted source and receiver planes by introducing the space- and time-lag variables

$$\mathbf{p}_s\cdot(\mathbf{x} + \boldsymbol{\lambda}) = v\,(t + \tau) \ , \tag{22}$$

$$\mathbf{p}_r\cdot(\mathbf{x} - 2d\mathbf{n} - \boldsymbol{\lambda}) = v\,(t - \tau) \ . \tag{23}$$

Solving the system of equations 22-23 leads to the expression

$$(\mathbf{p}_s - \mathbf{p}_r)\cdot\mathbf{x} = 2v\tau - (\mathbf{p}_s + \mathbf{p}_r)\cdot\boldsymbol{\lambda} - 2d\mathbf{p}_r\cdot\mathbf{n} \ , \tag{24}$$

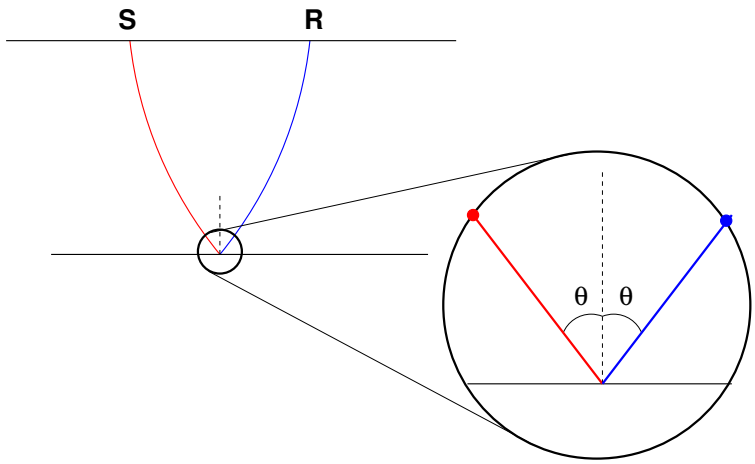


Figure 4. Cartoon describing wave propagation in an inhomogeneous medium. The wavepaths in the local region around the reflection point can be approximated with straight lines.

which characterizes the moveout at an image point function of space- and time-lags.

On the other hand, we have the following relations for the reflection geometry:

$$\mathbf{p}_s - \mathbf{p}_r = 2\mathbf{n} cos\theta \,, \tag{25}$$

$$\mathbf{p}_s + \mathbf{p}_r = 2\mathbf{q} sin\theta \,, \tag{26}$$

where $\mathbf{n}$ and $\mathbf{q}$ are unit vectors normal and parallel to the reflection plane, and θ is the reflection angle. Combining equations 24-25-26, we obtain a simplified moveout function for plane-waves:

$$z\left(\boldsymbol{\lambda},\tau\right) = d_0 - \frac{tan\theta\left(\mathbf{q}\cdot\boldsymbol{\lambda}\right)}{n_z} + \frac{v\tau}{n_z cos\theta} \,. \tag{27}$$

The quantity d_0 is defined as

$$d_0 = \frac{d - \left(\mathbf{c}\cdot\mathbf{n}\right)}{n_z} \,, \tag{28}$$

which represents the depth of the reflection corresponding to the chosen CIG location. Thus the quantity is invariant for different plane-waves, and it is used as a constant here.

When incorrect velocity is used for imaging, based on the analysis in the preceding section, we can obtain the moveout function

$$z\left(\boldsymbol{\lambda},\tau\right) = d_{0f} - \frac{tan\theta_m\left(\mathbf{q}_m\cdot\boldsymbol{\lambda}\right)}{n_{mz}} + \frac{v_m\left(\tau - t_d\right)}{n_{mz} cos\theta_m} \,, \tag{29}$$

where d_{0f} is the focusing depth of the corresponding reflection point, v_m is the migration velocity, t_d is the focusing delay, $\mathbf{n}_m$ and $\mathbf{q}_m$ are the new normal and parallel vector to the reflector.

In this analysis, we derive the moveout functions describing the extended images for a single seismic experiment. However, typical imaging employs multi-shot seismic experiments for better illumination of subsurface and analysis of the imaging redundancy which indicates velocity accuracy. Thus, it is important to understand the characteristics of the extended images in such situations and understand the moveout functions characterizing reflection experiments.

Since the wave equation is a linear partial differential equation, its solutions comply with the linear superposition principle . This is also true for the extended images, thus for multi-shot experiments the total extended images are the linear superimposition of the extended images from all the individual single-shot experiments. In this case, the moveout surface represents the envelope of the surfaces characterizing individual seismic experiments.

According to the definition, the envelope of a family of curves is obtained by setting both the implicit definition of the family and the derivative with respect to index parameter equal zero, and solving the system of equations. Therefore, the envelope representing a multi-shot image in extended CIGs with space-lag $\boldsymbol{\lambda}$ and time-lag τ is given by the system

$$G\left(z,\boldsymbol{\lambda},\tau,\theta\right) = 0 \,, \tag{30}$$

$$\frac{\partial G\left(z,\boldsymbol{\lambda},\tau,\theta\right)}{\partial\theta} = 0 \,, \tag{31}$$

where G represents the moveout function 27 for correct velocity and 29 for incorrect velocity, respectively. Solving the envelope system yields the following solutions:

$$z\left(\boldsymbol{\lambda},\tau\right) = d_0 + \frac{v\tau}{n_z}\sqrt{1 - \left(\frac{n_z\left(\mathbf{q}\cdot\boldsymbol{\lambda}\right)}{v\tau}\right)^2} \tag{32}$$

for correct velocity, and

$$z\left(\boldsymbol{\lambda},\tau\right) = d_{0f} + \frac{v_m\left(\tau - t_d\right)}{n_{mz}}\sqrt{1 - \left(\frac{n_{mz}\left(\mathbf{q}_m\cdot\boldsymbol{\lambda}\right)}{v_m\left(\tau - t_d\right)}\right)^2} \tag{33}$$

for incorrect velocity.

Analyzing the envelope functions for the cases of correct and incorrect velocities, we note that both envelope functions share a similar form, thus they should have similar properties. The envelope functions become singular when $\tau = 0$ or $\tau = t_d$, because at these special time-lags, all the individual surfaces corresponding to various experiments intersect at the same location. Mathematically, the envelope function is equivalent to a delta function at this τ, which represents a singularity. Also, the square-root term in the formula contains a subtraction, thus we have to ensure that the content under the square-root is non-negative otherwise the formula fails. This implies that the range of variable $\boldsymbol{\lambda}$ is limited which suggests

that we need to restrict the range of $\boldsymbol{\lambda}$ when we measure the moveout of the reflections.

Given the envelope functions shown in equations 32-33, we conclude that the envelope surface forms a "light cone", as shown in Figures 5(a) and 5(b), corresponding to correct and incorrect velocities respectively, for a horizontal reflector and in Figures 5(c) and 5(d) for a dipping reflector. The shapes of the cones change both with velocity and with reflector dip angle. The cones are incomplete due to the limitations of acquisition aperture. When velocity is correct, the origin of the cone is located at zero time-lag and at the same depth of the reflection point. In contrast when velocity is incorrect, the light cone is shifted in both space and time. The shift in time is exactly the focusing delay t_d defined before and the location of the shifted origin is the focusing depth d_{0f}.

If we slice the light cone at negative time-lags, the slices correspond to the region before the origin, thus these events are shaped like a frown, as indicated by the thick line in the plot. In contrast, the slices corresponding to the region after the origin are shaped like a smile .The events present in the zero time-lag slice in the case of incorrect velocity are characterized by the residual moveout used in more conventional migration velocity analysis (Sava & Biondi, 2004a,b). By examining the position of the origin of the light cone, we can asses the accuracy of the velocity model. If the origin occurs at zero time-lag, the velocity model is correct. If the origin shifts to non-zero time-lags, then the migration velocity is incorrect. Thus the position of the origin of the light cone can be used as a velocity error indicator.

To summarize, for inhomogeneous media, no analytic moveout function exists to describe moveout surfaces of the extended images. However, by restricting the observation in the vicinity of the reflection point, and by assuming that the velocity change above the image points is relatively uniform, we can use plane-wave approximation to describe the analytic functions characterizing extended images. The parameters describing the moveout functions, though, represent a combination of the velocity errors accumulated along the wave propagation paths, similarly to the case of traveltime errors used for conventional traveltime tomography.

5 EXAMPLES

We illustrate the validity of the moveout functions derived in the preceding sections with several synthetic models. The first model consists of a horizontal reflector embedded in a constant velocity medium, while the second model also consists of a constant velocity medium, but with a dipping reflector. We use the first model to verify the accuracy of the moveout function for point sources, and use the second model to verify the accuracy of the moveout functions for plane-wave sources. The extended images are generated with both the correct and incorrect velocities. The incorrect velocity is obtained by scaling the correct velocity with a constant factor.

The image corresponding to the correct and incorrect velocities are shown in Figures 6(a) and 6(b), respectively. The extended images are constructed at CIG location $c_x = 0.75$ km. Thus, for a source located at $x = 4.5$ km, the CIGs analyzed are located at $x = 5.25$ km. To verify the accuracy of the moveout function, we overlay the analytic moveout function on extended images at either fixed time-lags or at fixed horizontal space-lags.

Figures 7(a)-7(c) and 7(d)-7(f) depict space-lag gathers corresponding to the chosen CIG location for correct and incorrect velocities, respectively. From left to right, the panels correspond to slices at $\tau = \{-0.20, 0, +0.20\}$ s. In each column, the upper panel corresponds to correct velocity while the lower panel corresponds to incorrect velocity. The dashed line overlain on each panel corresponds to the analytic functions $z(\lambda_x, \tau)$ derived earlier. Notice that at $\tau = 0$, the moveout event is linear for correct velocity and nonlinear for incorrect velocity, as expected. For time-lag gathers, Figures 8(a)-8(c) and 8(d)-8(f) depict time-lag gathers corresponding to the chosen CIG location for correct and incorrect velocities, respectively. From left to right, the panels correspond to $\lambda_x = \{-0.4, 0, +0.4\}$ km. In each column, the upper panel corresponds to correct velocity while the lower panel corresponds to incorrect velocity. The dashed line overlain on each panel corresponds to the analytic functions $z(\lambda_x, \tau)$ derived earlier. In both cases, the analytic formula accurately describes the moveout surface characterizing extended images, which illustrates the validity of the moveout function in both correct and incorrect velocity.

Figures 9(a) and 9(b) show the migrated images of the dipping reflector corresponding to correct and incorrect velocity, respectively. To obtain the images, we use 40 shots equally spaced on the surface and stack the images from all individual shots. As discussed before, the moveout surfaces correspond to the superposition of the surfaces obtained for individual shots. We choose $x = 4.5$ km as the CIG location. Figures 10(a)-10(f) depict the moveout surfaces at different time-lags. From left to right, the upper panels display the slices at $\tau = \{-0.15, 0.0, +0.15\}$ s. The lower panels correspond to the same slices but overlain with the derived analytic envelope function. The dash line overlain on each panel correspond to $z(\lambda_x, \tau)$ given by equation 32 at various τ. As expected, all the events intersect at the same location at zero space- and time-lag since the correct velocity is used for imaging. For incorrect velocity, the light cones shift and thus their origin is not located at zero time-lag. The slice at zero time-lag is thus a curved event. Figures 11(a)-11(f) depict envelope of the moveout surfaces at different time-lags. From left to right, the upper panels display the slices of the light at $\tau = \{-0.15, 0.0, +0.15\}$ s. The lower panels correspond to the same slices but overlain with the derived analytic envelope function. The dashed line overlain on each panel corresponds to $z(\lambda_x, \tau)$ given by equation 33 at various τ. The slice at zero time-lag shows a curved event rather than a focused point, which demonstrates the shift of the origin of the light cone. The slice at $\tau = 0.15$ s shows a focused point, which is the origin of the light cone. In both correct and incorrect velocities, the analytic functions perfectly match the obtained envelope, which demonstrates the accuracy of the formulas in the description of the envelope.

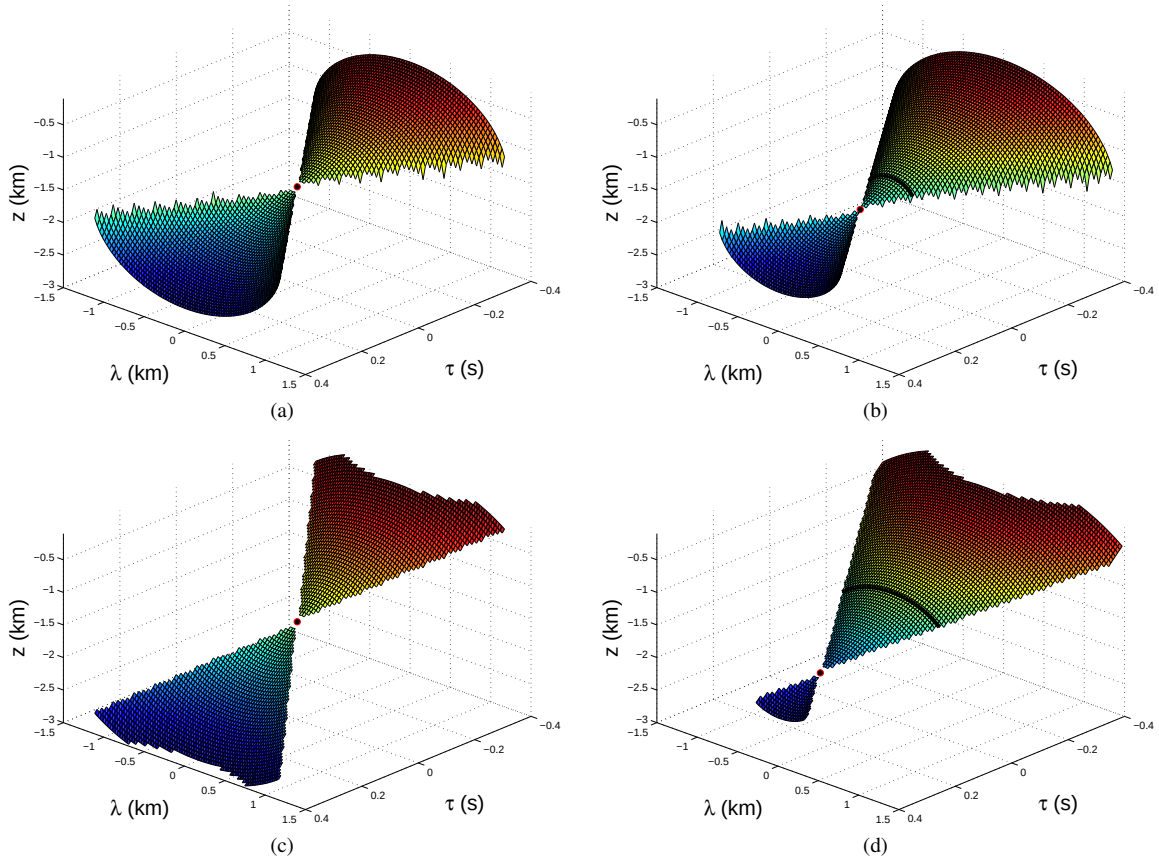
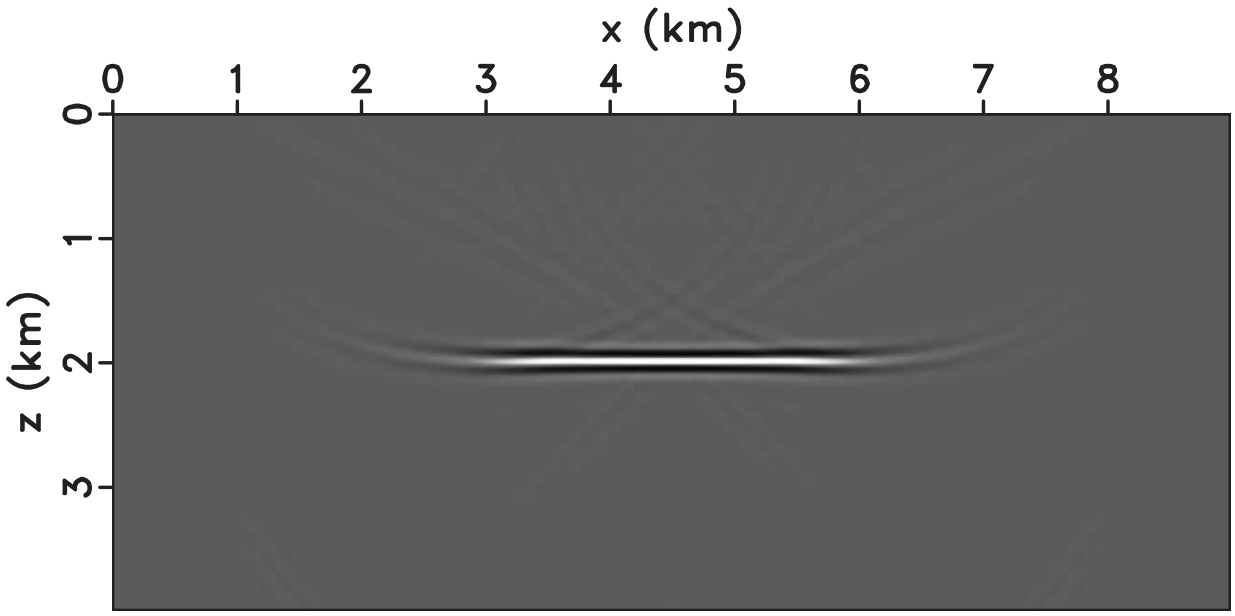
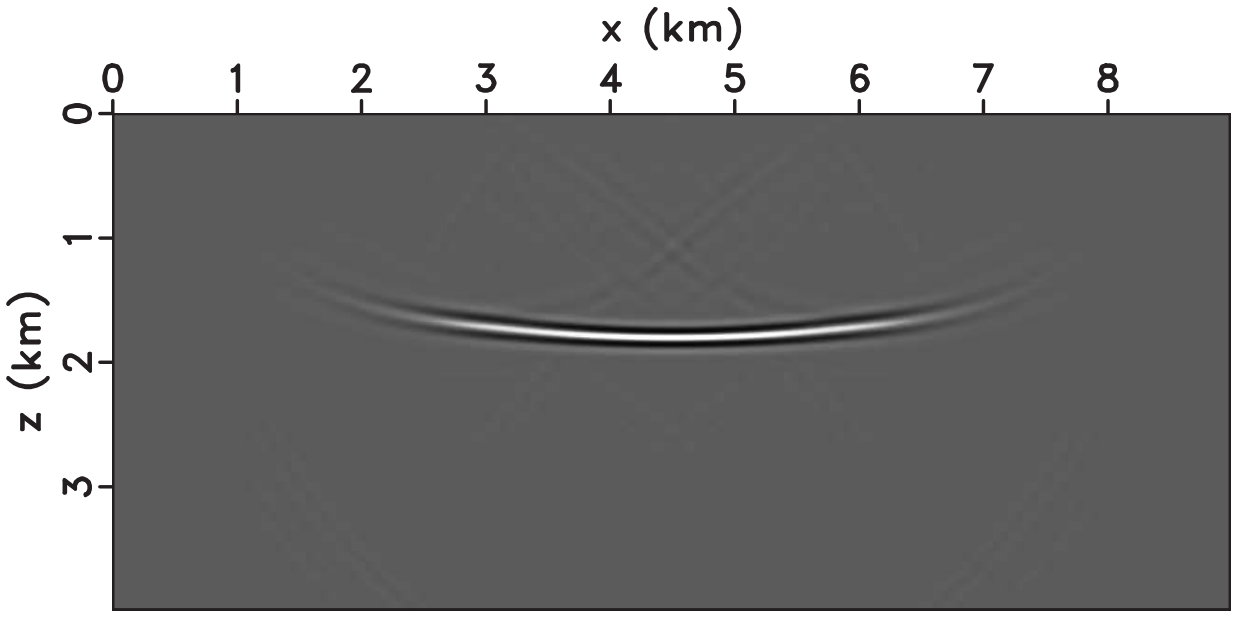


Figure 5. Light cone formed by the envelope of the moveout surfaces corresponding to individual plane-waves for a horizontal reflector in (a) the correct velocity case, the focus of the cone occurs at zero space- and time-lags and (b) the incorrect velocity case, the focus of the cone shifts to a nonzero time-lag. Light cone formed by the envelope of the moveout surfaces corresponding to individual plane-waves for a dipping reflector in (c) the correct velocity case, the focus of the cone occurs at zero space- and time-lags and (d) the incorrect velocity case, the focus of the cone shifts to a nonzero time-lag. The thick line corresponds to the slice of the cone cut at zero time-lag.



(a)



(b)

Figure 6. Migrated image corresponding to (a) correct velocity and (b) incorrect velocity.

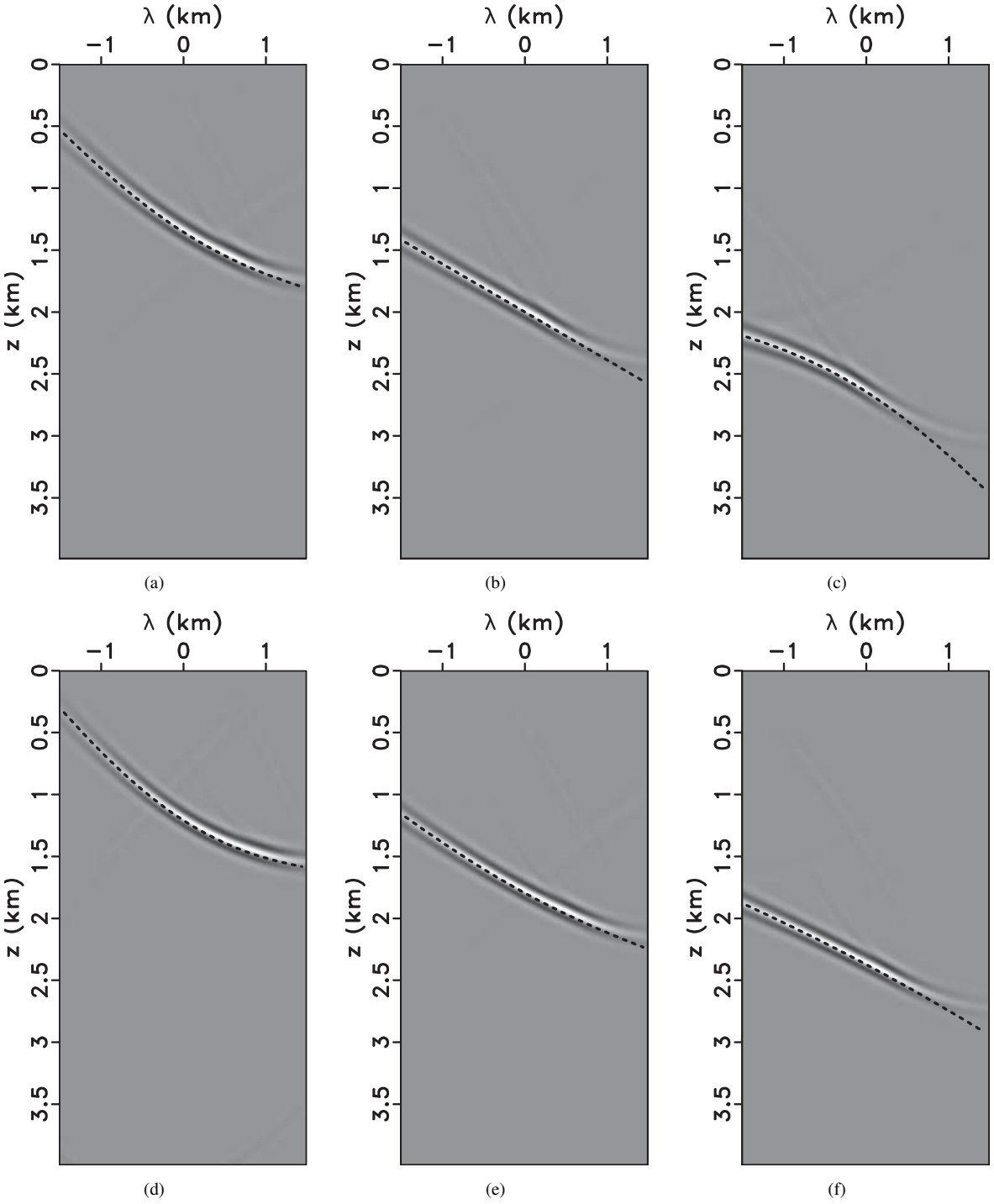


Figure 7. Space-lag CIGs for $\tau = \{-0.20, 0, +0.20\}$ s. Panels (a)-(c) correspond to correct velocity. Panels (d)-(f) correspond to incorrect velocity. The dash line overlain corresponds to the derived analytic function.

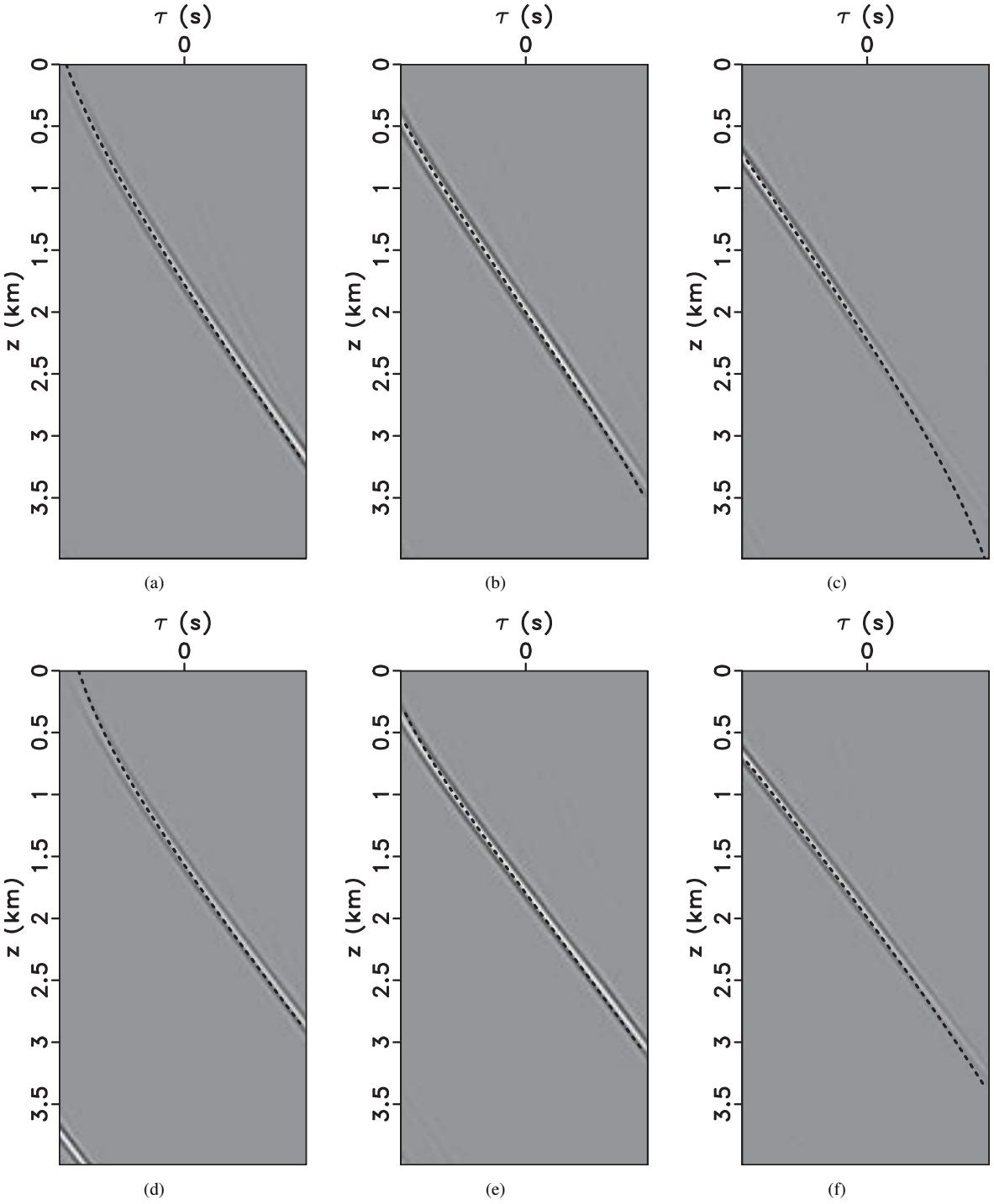
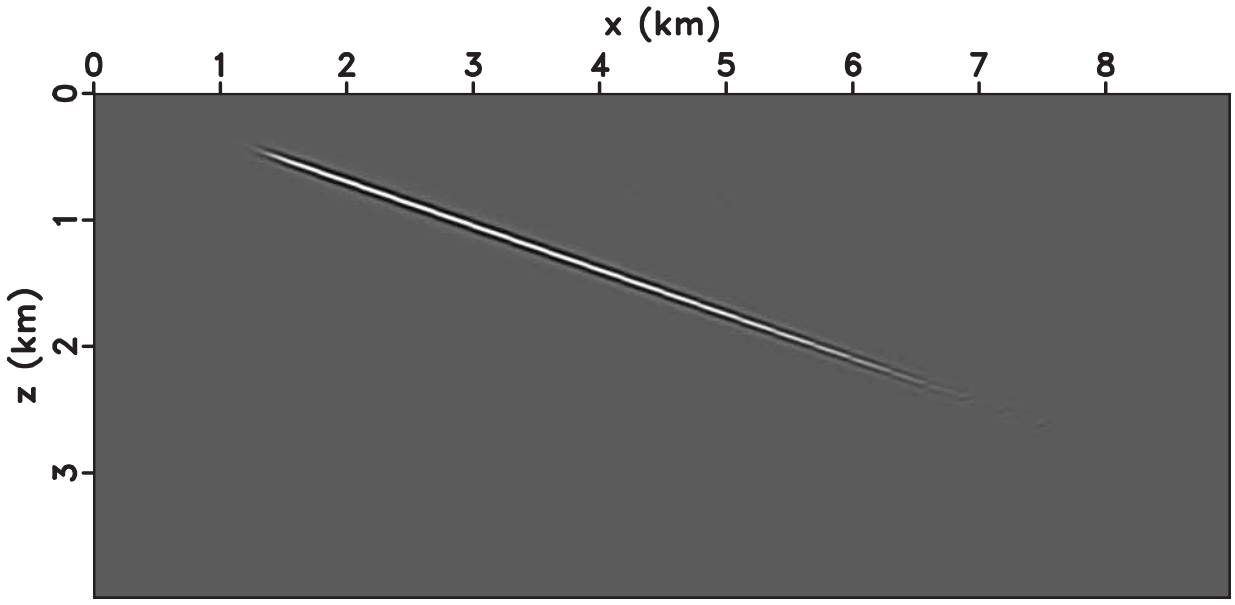
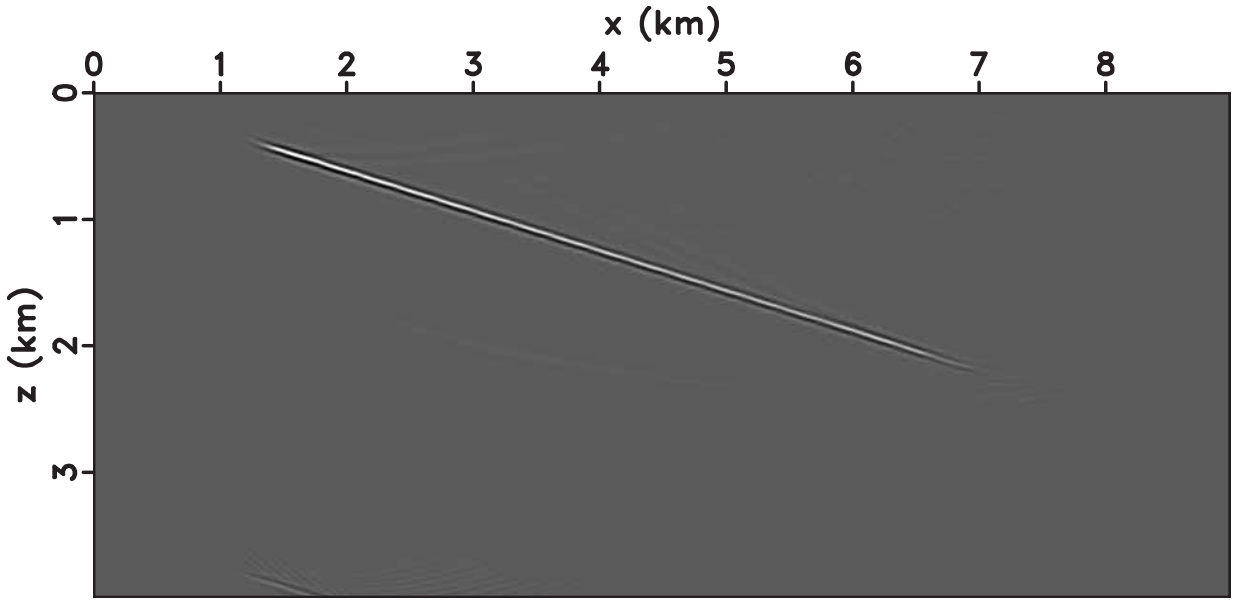


Figure 8. Time-lag CIGs for $\lambda_x = \{-0.4, 0, +0.4\}$ km. Panels (a)-(c) correspond to correct velocity. Panels (d)-(f) correspond to incorrect velocity. The dash line overlain corresponds to the derived analytic function.



(a)



(b)

Figure 9. Migrated image corresponding to (a) correct velocity and (b) incorrect velocity.

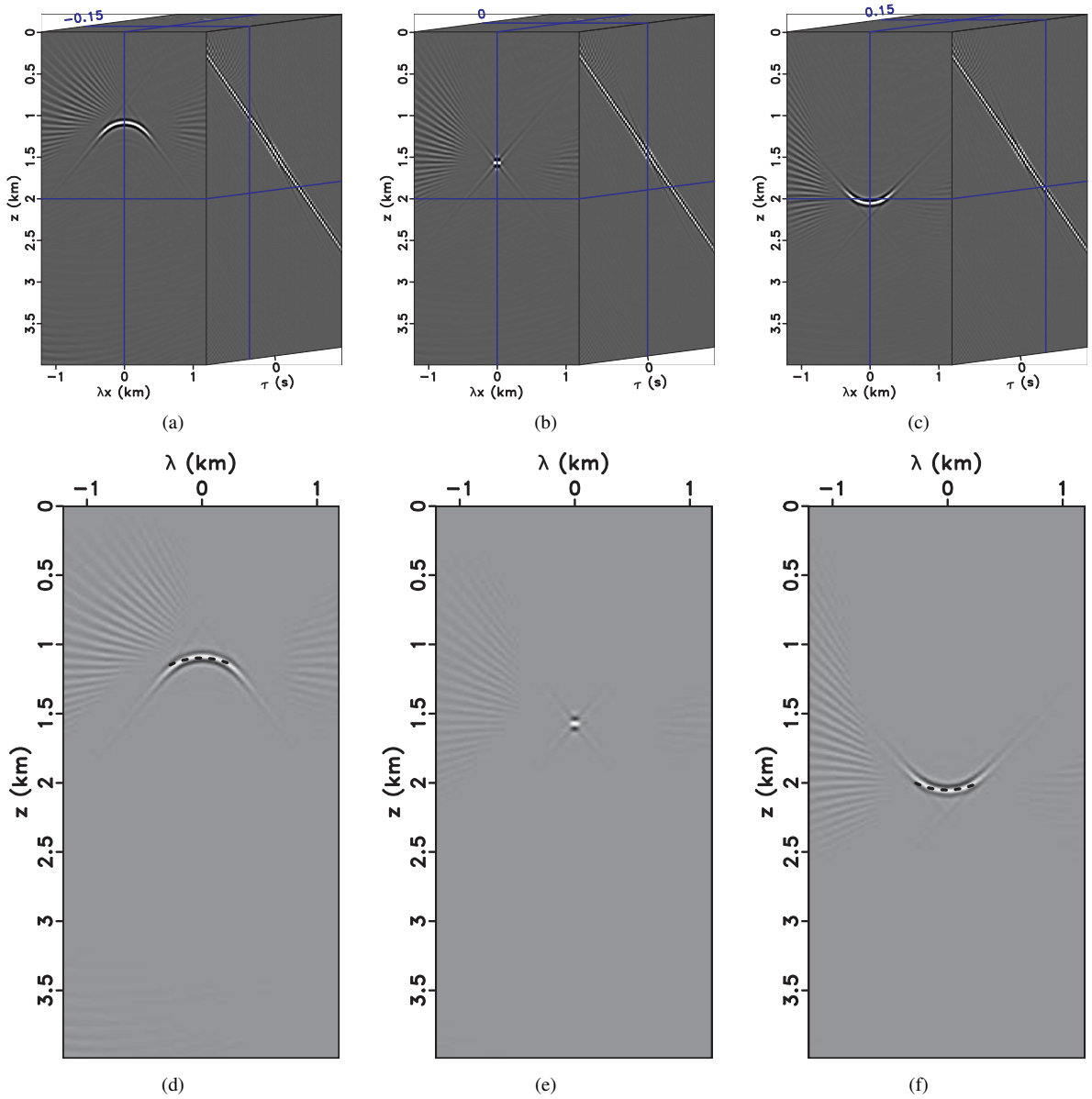


Figure 10. Envelope of the moveout surfaces at different time-lag for correct velocity. Panels (a)-(c) correspond to slices at $\tau = \{-0.15, 0, +0.15\}$ s, respectively. Panels (d)-(f) show the same slices overlain by the derived analytic envelope function.

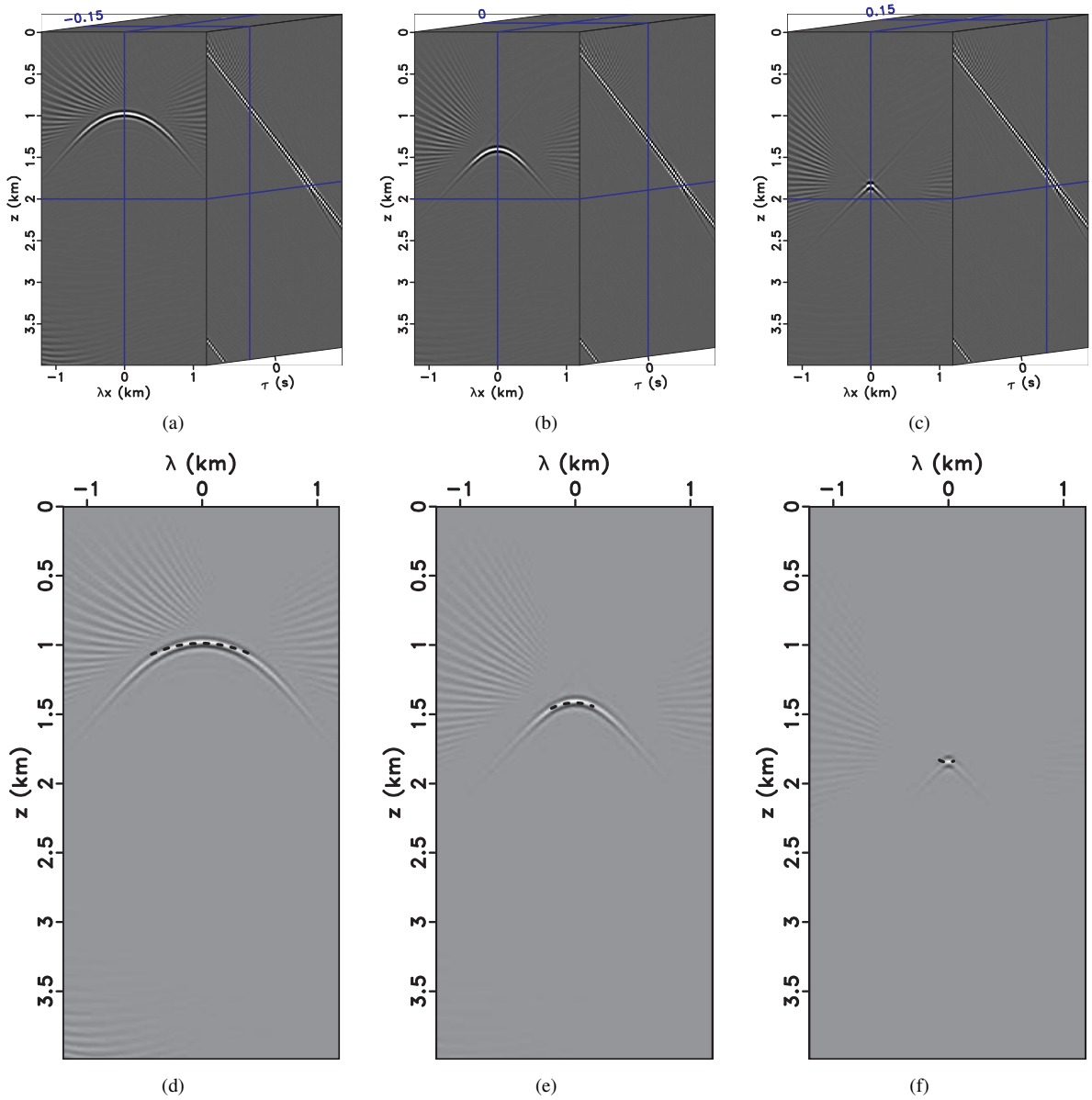


Figure 11. Envelope of the moveout surface at different time-lag for incorrect velocity. Panels (a)-(c) correspond slices to $\tau = \{-0.15, 0, +0.15\}$ s, respectively. Panels (d)-(f) show the same slices overlain by the derived analytic envelope function.

Finally, we use the Sigsbee model to illustrate the application of our technique to inhomogeneous media. Figures 12(a) and 12(b) show the correct velocity model and the migrated image. The sources are distributed over the left area of the model, thus they illuminate mainly the left side of the image. Figures 13(a) and 13(b) show the incorrect velocity model and the corresponding migrated image. The reflectors are mispositioned and defocused due to the incorrect velocity.

Figures 14(a) and 14(b) depict the moveout surfaces at different time-lags for the case of imaging with correct velocity. The panels correspond to slices of the light cone at different time-lags. Figure 14(a) shows the slice at $\tau = -0.15$ s. The events in the panel frowns down since the slice is cut at negative τ. Figure 14(b) shows the slice at $\tau = 0.0$ s, which is cut at the origin of the light cone. The events in the panel appear focused at zero time-lag and space-lag, indicating correct velocity.

Figures 15(a) and 15(b) depict moveout surfaces at different time-lags for the case of imaging with incorrect velocity. The panels correspond to slices of the light cone at different time-lags. Since the migration velocity is higher than the true velocity, the origin of the light cone is expected to shift to negative τ. Figure 15(a) shows the slice at $\tau = -0.15$ s. The events in the panel focus at zero space-lag, which means that the slice is cut at the origin of the light cone. Deeper events have the focus of the light cone at other values of τ. Figure 15(b) show the slices at $\tau = 0.0$ s. The events in the panels smile up because the slice is cut away from the focus of the light cone.

6 CONCLUSIONS

Extended imaging condition offers the possibility to design robust migration velocity analysis methods which simultaneously exploit conventional semblance analysis and depth focusing analysis. The moveout functions characterizing the extended images are non-planar analytic surfaces which naturally reduce to the conventional space-lag and time-lag moveout functions.

The analytic moveout functions allows quantitative description of the shape of the extended images. The envelope of the movoeout function characterizing the common image gathers constructed from multiple seismic experiments form light cones in the depth-lags domain. The origin of the light cone represents a well focused image of the reflector. If the velocity is correct, the origin locates at zero time-lag, otherwise the origin moves to nonzero time-lags and to an incorrect depth. The characteristic can be used as a velocity error indicator for tomographic techniques. Synthetic examples verify the validity of the analytic moveout functions and demonstrate that the properties of the light cones hold even in complex media.

7 ACKNOWLEDGMENTS

This work is supported in part by the sponsors of the Center for Wave Phenomena at Colorado School of Mines and by a research grant from StatoilHydro.

REFERENCES

Biondi, B., and Symes, W., 2004, Angle-domain common-image gathers for migration velocity analysis by wavefield-continuation imaging: Geophysics, **69**, 1283–1298.

Claerbout, J. F., 1985, Imaging the Earth's interior: , Blackwell Scientific Publications.

Faye, J. P., and Jeannot, J. P., 1986, Prestack migration velocities from focusing depth analysis: Prestack migration velocities from focusing depth analysis:, Soc. of Expl. Geophys., 56th Ann. Internat. Mtg., Session:S7.6.

Fomel, S., 2004, Theory of 3-D angle gathers in wave-equation imaging: 74th Annual International Meeting, SEG, Soc. of Expl. Geophys., Expanded Abstracts, 1053–1056.

MacKay, S., and Abma, R., 1992, Imaging and velocity estimation with depth-focusing analysis: Geophysics, **57**, no. 12, 1608–1622.

MacKay, S., and Abma, R., 1993, Depth-focusing analysis using a wavefront-curvature criterion: Geophysics, **58**, no. 08, 1148–1156.

Nemeth, T., 1995, Velocity estimation using tomographic depth-focusing analysis: Velocity estimation using tomographic depth-focusing analysis:, Soc. of Expl. Geophys., 65th Ann. Internat. Mtg, 465–468.

Nemeth, T., 1996, Relating depth-focusing analysis to migration velocity analysis: Relating depth-focusing analysis to migration velocity analysis:, Soc. of Expl. Geophys., 66th Ann. Internat. Mtg, 463–466.

Rickett, J., and Sava, P., 2002, Offset and angle-domain common image-point gathers for shot-profile migration: Geophysics, **67**, no. 3, 883–889.

Sava, P., and Biondi, B., 2004a, Wave-equation migration velocity analysis - I: Theory: Geophysical Prospecting, **52**, 593–606.

——— 2004b, Wave-equation migration velocity analysis - II: Subsalt imaging examples: Geophysical Prospecting, **52**, 607–623.

Sava, P. C., and Fomel, S., 2003a, Angle-domain common-image gathers by wavefield continuation methods: Geophysics, **68**, no. 3, 1065–1074.

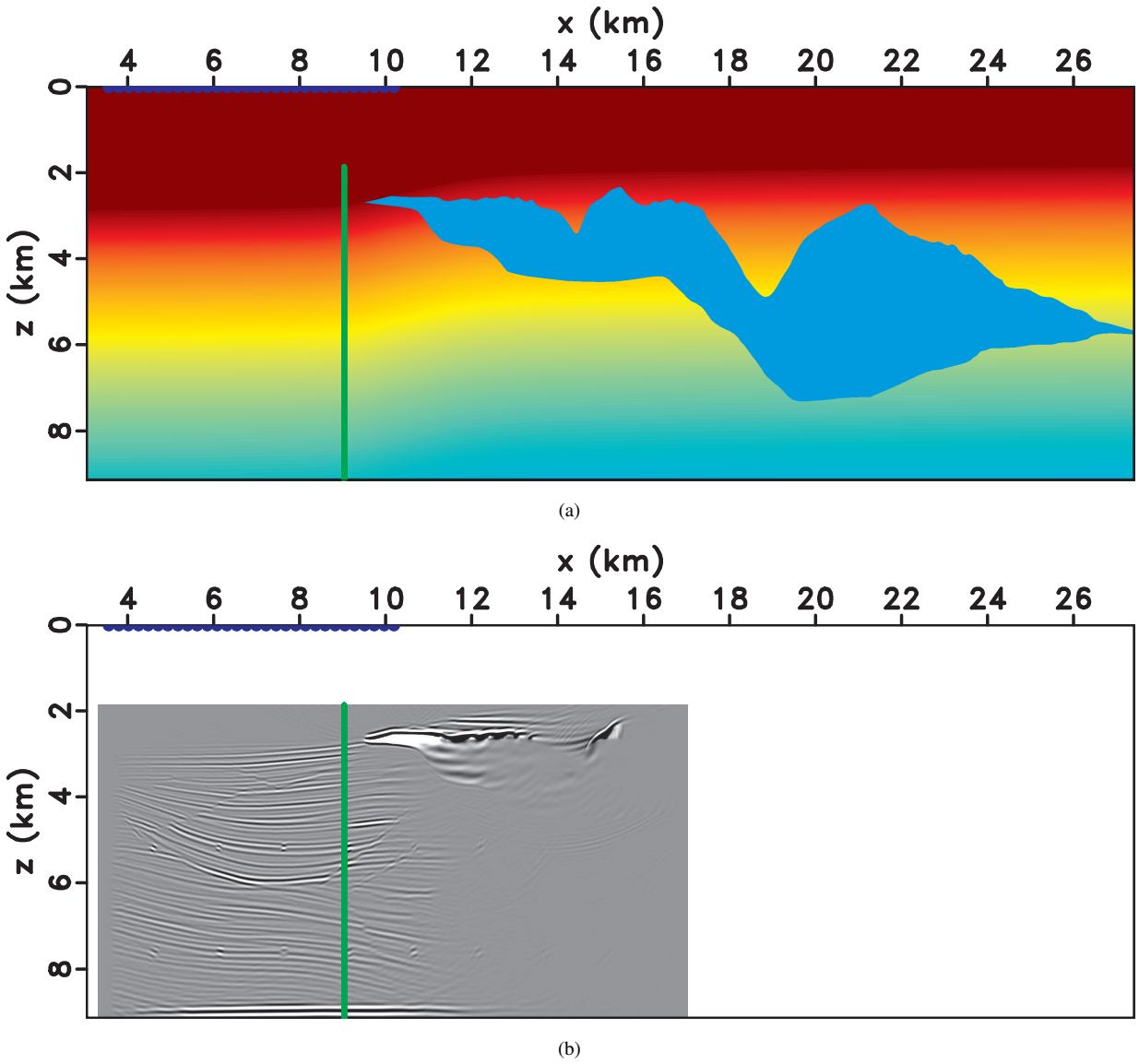
——— 2003b, Angle-domain common image gathers by wavefield continuation methods: Geophysics, **68**, no. 3, 1065–1074.

Sava, P., and Fomel, S., 2006, Time-shift imaging condition in seismic migration: Geophysics, **71**, no. 6, S209–S217.

Shen, P., Symes, W., Morton, S., and Calandra, H., 2005, Differential semblance velocity analysis via shot profile migration: 74th Annual International Meeting, SEG, Expanded Abstracts, 2249–2253.

Stolk, C. C., and Symes, W. W., 2004, Kinematic artifacts in prestack depth migration: Geophysics, **69**, no. 2, 562–575.

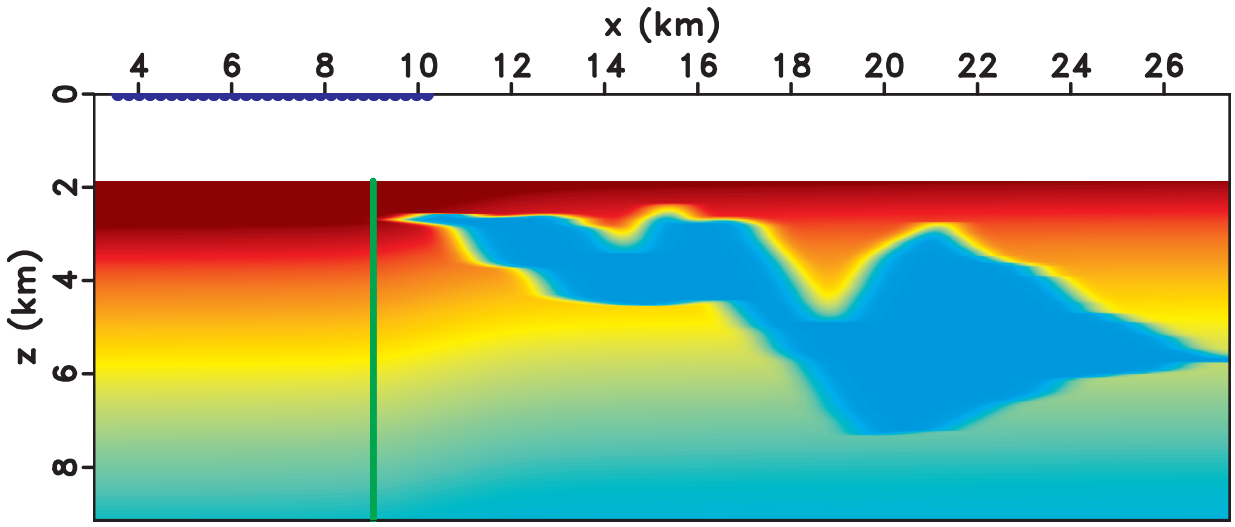
Yilmaz, O., 2001, Seismic Data Analysis (2nd edition): , Society of Exploration Geophysicists.



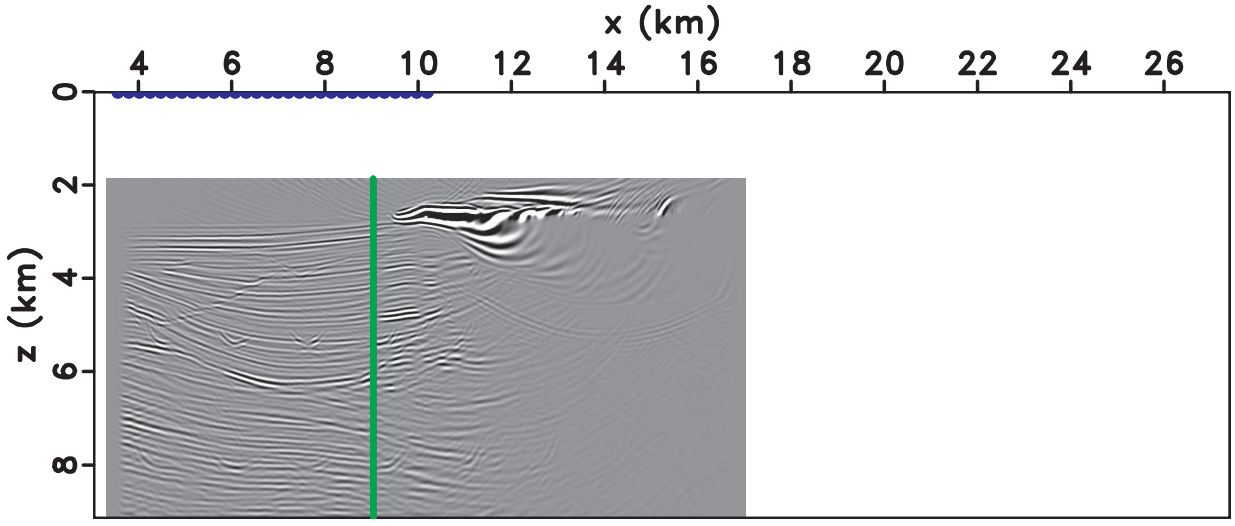
(a)

(b)

Figure 12. Sigsbee model. (a) correct velocity model and (b) corresponding image.



(a)



(b)

Figure 13. Sigsbee model. (a) incorrect velocity model and (b) corresponding image.

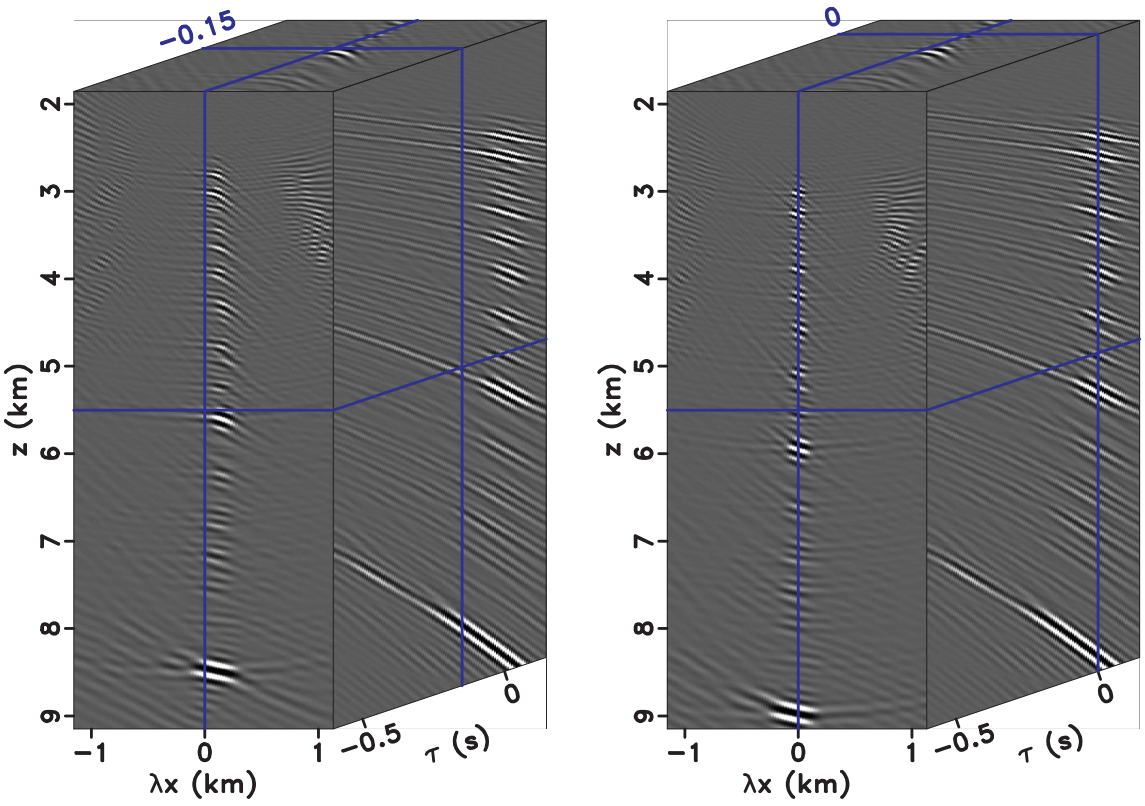


Figure 14. Moveout surface at different time-lags for correct velocity. Panels (a) and (b) correspond to slices of the light cone at $\tau = \{-0.15, 0\}$ s, respectively.

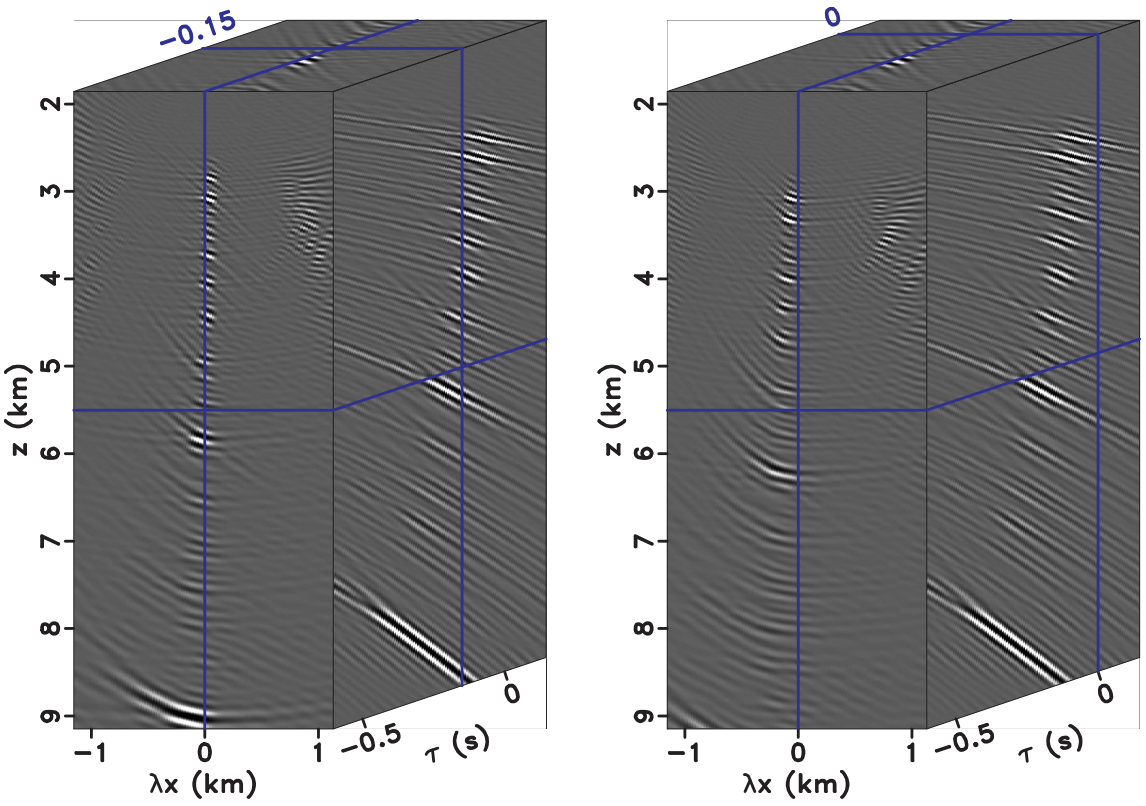


Figure 15. Moveout surface at different time-lags for incorrect velocity. Panels (a) and (b) correspond to slices of the light cone at $\tau = \{-0.15, 0\}$ s, respectively.